1   **Temporal variations of the hygroscopicity and mixing state of black**

2   **carbon aerosols in a polluted megacity area**

3   Kangning Li[1], Xingnan Ye[1], Hongwei Pang[1], Xiaohui Lu[1], Hong Chen[1], Xiaofei

4   Wang[1,2]*, Xin Yang[1,2]*, Jianmin Chen[1], Yingjun Chen[2,3]

5   *[1]Shanghai Key Laboratory of Atmospheric Particle Pollution and Prevention, Department of*

6   *Environmental Science and Engineering, Fudan University, Shanghai 200433, China*

7   *[2]Shanghai Institute of Pollution Control and Ecological Security, Shanghai 200092, China*

8   *[3]College of Environmental Science and Engineering, Tongji University, Shanghai 200092,*

9   *China*

10   Correspondence to: Xiaofei Wang (xiaofeiwang1986@gmail.com); Xin Yang

11   (yangxin@fudan.edu.cn)

13   **Keywords**: aerosol, black carbon, hygroscopicity, mixing state, SP2

15   **Abstract.**

16   Black carbon (BC) aerosols in the atmosphere strongly affect radiative forcing. They

17   are mainly removed from the air by wet deposition, and their lifetime is controlled by

18   their water uptake ability or hygroscopicity, which is a function of the aerosol mixing

19   states. It is well known that atmospheric aging processes coat various materials on BC

20   aerosols and affect their mixing states and hygroscopicity. However, detailed relations

21   between the aging processes, the hygroscopicity and mixing state of BC aerosol

22   particles in polluted city areas are not well understood. Here, we studied the temporal

23   variation of the hygroscopicity and its correlation with the mixing state of ambient BC

24   particles during 2017 summer in Shanghai, China using a hygroscopicity tandem

25   differential mobility analyzer in-line with a single particle soot photometer

26   (HTDMA-SP2 system) as well as a single particle aerosol mass spectrometer

27   (SPAMS). BC particles with 120 nm, 240 nm and 360 nm dry diameter were

28   humidified at RH=85%. After humidification, particles with growth factors (GFs) of

29   1.0, 1.2 and 1.4, representing the BC particles with different hygroscopicities

30   (hydrophobic, transition and hydrophilic modes, respectively), were analyzed by a

31   SP2 to obtain their BC mixing states. The diurnal trends of coating thickness and

32   chemical mixing state show that coating materials of BC particles were distinct

33   between daytime and nighttime. The differences were associated with the

34   hygroscopicity of BC particles. Single particle mass spectrometry and other chemical

35   characterization techniques revealed that during nighttime with lower temperature and

36   higher relative humidity (RH), formation or condensation of nitrates resulted in an

37   enhanced hygroscopicity of BC particles. During daytime, secondary organic carbon

38   formation was mainly responsible for the change of hygroscopicity of BC particles.

39   Due to the high hygroscopicity of inorganic nitrate, a thinner nitrate coating on BC

40   particles could convert fresh BC particles to aged hygroscopic ones during nighttime

41   while a thicker coating layer of secondary materials was required to reach the same

42   overall hygroscopicity during daytime since the participation of secondary organic

43   carbon. Different atmospheric aging processes between daytime and nighttime led to

44   the change of BC particles' mixing states, which play a fundamental role in

45   determining their hygroscopicity. To our knowledge, this is the first report of links

46   between temporal variations of the hygroscopic growth of BC particles and

47   atmospheric aging processes in polluted environment. These findings have significant

48   ramification of understanding the aging process, wet removal as well as climate

49   effects of BC particles.

1 Introduction

Black carbon (BC) aerosols are a strong light absorbing component in the atmosphere and a major contributor to the positive radiative forcing (Bond et al., 2013) (Change, 2015; Kondo, 2015). They are mainly generated from incomplete combustion of fossil fuels and biomass. Freshly emitted BC particles are hydrophobic. However, their hygroscopicity can be enhanced by internally mixing with secondary materials through atmospheric aging processes (Schneider et al., 2005; Shiraiwa et al., 2007; Matsui et al., 2013; Pratt et al., 2011). Hygroscopicity of BC aerosol significantly affects their removal rate through wet deposition, absorption in human's respiratory tract (Löndahl et al., 2007), optical properties (Chen et al., 2012), and their surface reactivity (Mogili et al., 2006). Therefore, it is critical to understand the relations between atmospheric aging processes and hygroscopicity of BC aerosols. In the atmosphere, an aerosol population typically consists of aerosol particles with various sizes and chemical compositions, which is usually described as "mixing state". The mixing state of atmospheric BC particles is closely linked to their sources and aging processes (Chirico et al., 2010; Heringa et al., 2011). Aerosol hygroscopicity are determined by the chemical compositions of each individual particle (McMeeking et al., 2011; Liu et al., 2013). Thus, aerosol mixing states play a critical role in determining the hygroscopicity of BC particles.

The relations between the hygroscopicity and mixing state of BC aerosols had been studied with many novel measurement techniques. Herich et al. (2008) combined an aerosol time of flight mass spectrometer (ATOFMS) with a hygroscopicity tandem differential mobility analyzer (HTDMA) to investigate the mixing state and hygroscopicity of BC-containing particles at an urban site in Zurich, Switzerland. It shows that most of BC-containing particles internally mixed with organics and combustion species (m/z $^{-26}CN^-$ and $^{-42}CNO^-$) have lower hygroscopicity compared with sulfate and nitrate mixed (Herich et al., 2008). A single particle soot photometer (SP2) was installed in downstream of HTDMA by Laborde

78 et al., which shows that the majority of urban aerosol particles with high

79 hygroscopicity (GF ≈ 1.6) do not contain a detectable refractory BC core while

80 hydrophobic or less hygroscopic particles ($1.1 \leq GF \leq 1.2$) have a BC core with no or

81 little coating of soluble species (Laborde et al., 2013). Similarly, by coupling a SP2

82 with a HTDMA, McMeeking et al. (2011) measured the hygroscopicity of ambient

83 BC particles externally and internally mixed BC particles using uncoated and coated

84 laboratory generated model BC particles. The obtained information is compared to the

85 hygroscopicity distribution of ambient BC aerosols. Their results suggest that the

86 dominant fraction of the BC particles is not readily act as cloud condensation nuclei

87 (CCN) at 0.2% super saturation in an urban area (McMeeking et al., 2011). By

88 coupling a HTDMA and an ATOFMS, our previous study finds that condensation of

89 amine and secondary inorganic species would enhance the hygroscopicity of

90 submicron particles, including BC particles (Wang et al., 2014). In addition, Liu et al.

91 (2013) deployed a similar instrument setup and investigated the relation between the

92 hygroscopic properties and mixing state of BC particles (Liu et al., 2013). It shows

93 that the GF of BC particles was influenced by the composition of soluble materials.

94 These previous studies have relied on real time hygroscopcity measurements, but

95 usually without detailed temporal information on changes of mixing state of BC

96 particles. Time resolved information on aerosol mixing state would be very useful to

97 identify their sources and aging processes. During summer time in heavily polluted

98 areas, the atmospheric aging processes could be much more complex due to higher

99 temperature, higher pollutants concentrations and stronger sunlight radiation.

100 However, according to our knowledge, few studies have reported time resolved

101 analysis on the mixing state and hygroscopicity of BC particles of particular GFs

102 during summer time. Therefore, with high time resolution single particle analysis, this

103 field study has aimed to determine the relations between BC particle hygroscopicity

104 and real time mixing state measurement in Shanghai, a heavily polluted megacity area.

105 It would provide more insights on the effects of atmospheric processes on

106   hygroscopicity of BC particles.

107   **2 Experimental section**

108   **2.1 HTDMA-SP2 system**

109   Temporal variation of BC aerosols mixing state and hygroscopic property were

110   measured using a custom-built HTDMA-SP2 system (Fig. 1). The HTDMA used in

111   this study is described in detail in our previous publications (Ye et al., 2009; Wang et

112   al., 2014). Brief descriptions about the instruments and their operations can be found

113   in the supplementary material. More details of SP2 data analysis are available in our

114   group's previous work (Gong et al., 2016).

115   Similar to those employed by Herich et al. (2008), Zelenyuk et al. (2008) and

116   Wang et al (2014), our HTDMA-SP2 system used a SP2 (DMT, Boulder, CO, USA)

117   in the downstream of a HTDMA to probe BC content as a function of hygroscopicity.

118   The first DMA in the HTDMA system selects monodisperse particles with a dry

119   particle diameter. Then the selected aerosols are humidified at a specified relative

120   humidity (RH=85% in this study). The size distribution of humidified (wet) particles

121   are measured by a scanning mobility particle sizer (SMPS), which includes another

122   DMA and a condensation particle counter (CPC, model 3771, TSI Inc.). GF is the

123   ratio between particle wet size and dry size. The SP2 identifies BC-containing

124   particles at each selected GF. The water uptake properties of BC particles can be

125   linked directly to the mixing state measured by SP2.

126   In this study, aerosol particles with three electrical mobility sizes (120 nm, 240

127   nm and 360 nm in dry diameter) are selected. After humidification, particles with

128   growth factors (GFs) of 1.0, 1.2 and 1.4, representing particles with different

129   hygroscopicities, which are defined as (1) hydrophobic, (2) transition and (3)

130   hydrophilic mode, respectively.

131   **2.2 Single particle aerosol mass spectrometer (SPAMS)**

132   A single particle aerosol mass spectrometer (SPAMS Hexin Analytical

133   Instrument Co., Ltd., China) was used in parallel to the HTDMA-SP2 system. The

134   SPAMS first measures the size of a single aerosol particle. Then, it uses a 266 nm

135   laser to disintegrate the particle and ionize its chemical compounds, of which

136   mass-to-charge ratios (m/z) and concentration are determined by a bipolar

137   time-of-flight mass spectrometer. Detailed information on the SPAMS has been

138   described elsewhere (Li et al., 2011).

139   In this work, a total of 158,410 individual particle mass spectra were collected,

140   accounting for about 56% of all the particles that were sized in the SPAMS. Element

141   carbon ion clusters has been considered an important marker for BC aerosols (Gong et

142   al., 2016). Using $C_n^{+/-}$ (n=1, 2, 3…) as the BC marker, a total of 64,368 BC-containing

143   particles were identified, accounting for about 40.1% of sampled particles. The mass

144   spectra of BC-containing particles were classified into several types based on their

145   similarities using a clustering algorithm called adaptive resonance theory (ART-2a)

146   (Song et al., 1999). Similar to previous studies (Huang et al., 2013; Zhai et al., 2017)

147   (Gong et al., 2016; Spencer et al., 2007), the vigilance factor, learning rate, and

148   iterations for ART-2a algorithm were set to 0.85, 0.05, and 20, respectively. Finally,

149   five particle types were manually combined based on the similarity of their chemical

150   nature.

151   Noticeably, the particles with mobility size at 120 nm cannot be detected by the

152   SPAMS, as they were smaller than the lower limit (200 nm) of size range of the

153   SPAMS. According to Slowik's study, the vacuum aerodynamic diameter (d_{va}) of

154   compact aggregated BC particles was linearly proportional to mobility diameter (d_m),

155   specifically, $d_{va} = 1.3*d_m$ (Slowik et al., 2004). Here we assume that most detected BC

156   particles follows this relation ($d_{va} = 1.3*d_m$). In this study, only particles with $D_0 =$

157   120 nm, 240 nm and 360 nm were studied with the HTDMA-SP2 system. These

158   mobility sizes correspond to d_{va} = 150 nm, 312 nm and 468 nm, respectively. Thus,

159   the SPAMS cannot provide mixing state information for particles with d_{va} = 150 nm

160   (d_m = 120 nm), which was out of the SPAMS detection range (200 to 2000 nm).

161   **2.3 Other instruments**

162   **2.3.1 OC/EC analyzer**

163   Hourly mass concentrations of elemental carbon (EC) and organic carbon (OC)

164   were measured by a semi-continuous OC/EC analyzer (Model 4, Sunset Laboratory

165   Inc., Portland, USA.) based on the National Institute of Occupational Safety and

166   Health thermal/optical transmittance measurement protocol (NIOSH 5040), with a

167   PM$_{2.5}$ impactor inlet. Detailed information can be found in the previous publication

168   (Wang et al., 2016a). Concentration of secondary organic carbon (SOC) was

169   estimated using the method of minimum ratio of OC/EC (Chou et al., 2010), which is

170   calculated by the following equation.

171    $$SOC = OC_{total} - EC \times (OC/EC)_{pri} \qquad (1)$$

172   where OC and EC are the measured hourly mass concentrations of organic

173   carbon and elemental carbon. (OC/EC)$_{pri}$ is the OC/EC ratio for primary aerosol

174   emission. At urban locations, the (OC/EC)$_{pri}$ was assumed to be the minimum value of

175   OC/EC ratio throughout the whole study sampling period (Cao et al., 2013). The OC

176   vs EC plot is displayed in Fig. S1. We use the minimum value 2.2 as the (OC/EC)$_{pri}$,

177   in this work.

178   **2.3.2 Monitor for Aerosols and Gases in Air (MARGA)**

179   A Monitor for Aerosols and Gases in Air (MARGA, Applikon Analytical B. B.

180   Corp., ADI 2080, Netherlands), with a PM$_{2.5}$ cyclone impactor, was deployed to

181   measure the concentrations of inorganic ionic species (i.e. SO_4^{2-}, NO_3^- and NH_4^+) in

182   PM$_{2.5}$. Detailed description about the MARGA is available in the previous publication

183   (Du et al., 2010).

184   **2.4 Sampling period and site**

185   The measurements of the relationship between mixing state and hygroscopicity

186   of BC particles various with time were carried out from 4 to 16 July 2017 using a

187   SPAMS and a HTDMA-SP2 system. The sampling site is located at the Department

188   of Environmental Science and Engineering in the main campus of Fudan University

189   (31.30ºN, 121.5ºE), and it is surrounded by residential and commercial areas. An

190   elevated road (the Middle Ring Line) with heavy traffic is ~ 400 m away from the

191   sampling location.

192   **2.5 Meteorology**

193   The meteorology and air quality information were obtained at a nearby air

194   quality monitoring station, which is operated by Shanghai Environmental Monitoring

195   Center (Yangpu Site). (http://www.semc.com.cn/aqi/home/Index.aspx). The station

196   was 3.3 km from the sampling site. Temporal profiles of measured gaseous pollutants

197   (O$_3$, SO$_2$, CO, and NO$_2$), temperature, relative humidity (RH), PM$_{2.5}$, and hourly PM$_{10}$

198   mass concentrations from July 4 to 16, 2017 are shown in Fig. 2. The temperature and

199   RH varied between 24.1ºC and 38.0 ºC, and 46% and 100%, with an average of 30.4

200   ºC, 74.1%, respectively, during the sampling period. Figure 2 shows that the

201   temperature was negatively correlated with RH, but positively correlated with O$_3$

202   mass concentration. Hourly O$_3$ concentration usually peaked in the afternoon during

203   this period. Its maximum value reached 316 μg/m^3 at 14:00 on July 12, showing

204   extremely active photochemical activities in this afternoon. The maximum value of

205   PM$_{2.5}$ reached 72 μg/m^3 at 18:00 on July 13, with an average of 29.2 μg/m^3.

206   Meanwhile, PM$_{10}$ varied from 15 to 141 μg/m^3, with an average of 57.9 μg/m^3.

207

3 Results and discussion

208

209   The focus of this paper is temporal variation of hygroscopicity and mixing states

210   of ambient BC particles. Due to the slow scanning rate of DMA voltage and sampling

211   time requirement of SP2, obtaining temporal information of BC concentrations

212   requires the DMA size selection to be fixed for a certain amount of time. Therefore,

213   for HTDMA-SP2 system, only one size (D_0) was studied for each sampling period.

214   Specifically, D_0 = 120, 240 and 360 nm was measured during 2017/07/04 06:00:00～

215   2017/07/07 05:00:00, 2017/07/07 06:00:00～2017/07/10 05:00:00 and 2017/07/10

216   06:00:00～2017/07/16 05:00:00, respectively.

217   We studied three GFs (GF=1.0, 1.2 and 1.4) for each D_0. The GF selection was

218   based on the GF size distribution of BC particles. A general picture of hygroscopicity

219   of total sampled ambient particles is shown in Fig. 3(a), which illustrates averaged

220   hygroscopic growth factor distributions at three selected sizes (D_0 = 120, 240 and 360

221   nm). All three GF curves featured a bimodal distribution, which contained a

222   hydrophobic mode peaks at GF = ~1.0 and a hydrophilic mode peaks at larger GFs

223   (1.3 ~ 1.6). Clearly, the hygroscopic particles were typically more abundant than the

224   hydrophobic ones. The hygroscopic growth distributions featured a size dependent

225   hygroscopic growth, significantly reducing of the particle number and shifting to

226   larger growth with increasing particle size, which were conventionally attributed to a

227   size dependent chemical composition (Swietlicki et al., 2008). In contrast,

228   hygroscopic growth factor distributions of BC particles only show one mode (Fig.

229   3(b)). The GF curve of BC particles peaked at GF = ~1.0. The BC-containing number

230   fraction decreased sharply for larger GFs. When GF was greater than 1.4, few BC

231   particles were detected by SP2.

232   GF=1.0, 1.2 and 1.4 was selected to represent hydrophobic, transition, and

233   hydrophilic mode for BC particles, respectively. Higher GFs (GF>1.4) were not

234   selected due to the low BC-containing number fractions at these GFs. For each day,

235   the sampling was divided to eight 3-hour sampling periods. Three GFs (GF=1.0, 1.2

236   and 1.4) were set sequentially for one hour during each sampling period.

237   Here, the diurnal trend (in Section 3.1) and classification (in Section 3.2) of BC

238   particles are described and discussed in detail. Then, the relations between mixing

239   state and hygroscopicity of BC particles are elucidated (in Section 3.3).

3.1 Diurnal variations of BC particles with different hygroscopicities

3.1.1 Diurnal variation of hydrophobic mode BC particles

242   The averaged diurnal patterns of the number concentration and number fraction

243   of BC particles are shown in Fig. 4(a) and 4(b), respectively. The number fraction of

244   BC particles is defined as the ratio of the number concentration of BC particles to that

245   of total ambient aerosol particles at a certain D_0 and GF. The majority of hydrophobic

246   mode (GF=1.0) BC particles typically exhibited two peaks for all three D_0s (Fig. 4(a)).

247   They were likely to be freshly emitted from combustion sources (McMeeking et al.,

248   2011). The number concentrations of hydrophobic BC particles reached their first

249   peak in the morning around 6:00 to 9:00 local time (LT), and then followed by a dip

250   in the afternoon around 12:00 to 17:00. The hydrophobic BC particles reached the

251   second peak in the evening and then slowly deceased during the night. This trend is

252   similar to some field studies in other city areas, such as Shenzhen and Xiamen in

253   China (Huang et al., 2012; Wang et al., 2016b). The elevated BC particle number

254   concentration in the morning and early evening can be explained by increases in local

255   anthropogenic emissions, especially those from rush hour traffic. This trend

256   presumably was also intensified by lower boundary layer heights at those times.

257   As shown in Fig. 4(b), hydrophobic BC particles accounted for the largest

258   percentage among three GFs for all D_0s. However, number fractions of hydrophobic

259   BC particles decreased with the increased D_0. For D_0 = 120 nm, 240 nm, 360 nm, the

260   maximum number fractions of hydrophobic BC particles were ~80%, 70% and 60%,

261 respectively. It is known that most of the fresh BC particles diameter are smaller than

262 200 nm (Kondo et al., 2006), which is consistent to our finding that relatively lower

263 fractions of BC particles were detected at larger sizes.

3.1.2 Diurnal variations of transition and hydrophilic mode BC particles

265   The transition and hydrophilic mode BC particles likely originated from aged

266 particles. Condensation of hydrophilic secondary materials (e.g. sulfate, nitrate and

267 secondary organic compounds) would significantly enhance the water uptake ability

268 of BC particles. As shown in Fig. 4(a), the number concentrations of some transition

269 and hydrophilic mode BC particles (like transition mode for 120 and 240nm BC

270 particles) showed a clear daily maximum during 12:00 ~ 15:00 (Fig. 4(a)). This trend

271 could be explained by the intense aging processes during this time when sunlight

272 intensity and atmospheric oxidants' concentration reach their peak values. However,

273 the number concentration of transition and hydrophilic mode BC particles could be

274 affected by other atmospheric aging processes. For example, nitrate formation could

275 be significantly enhanced during nighttime due to the hydrolysis of N_2O_5 (Wang et al.,

276 2009; Wang et al., 2016a). This process would make more transition and hydrophilic

277 mode BC particles during nighttime. To understand their diurnal trends, the

278 measurement of their chemical compositions and mixing states is essential, which will

279 be discussed in Section 3.3.

280   Fig. 4(b) also shows the diurnal variations of number fractions of transition and

281 hydrophilic mode BC particles. Contrast to the hydrophobic mode BC particles, the

282 transition and hydrophilic mode (GF = 1.2 and 1.4) BC particles with larger sizes

283 tended to contribute higher number fractions of total particles. It is known that BC

284 particles originated from traffic emissions are small (median diameter < 200 nm) (Xue

285 et al., 2015). Thus, the increased fraction of BC particles in $D_0 = 360$ nm hydrophilic

286 mode particles suggest these particles were from a different source. A candidate is

287 biomass burning (BB) aerosols, which have slightly higher hygroscopicity than those

288   from traffic emissions (Laborde et al., 2013). Detail discussion of BB aerosol will be

289   shown in Section 3.2.

290   In addition, the diurnal variations of BC particle number fraction showed that

291   during nighttime much larger proportion of BC particles were in hygroscopic mode

292   compared to daytime, indicating that hygroscopicity of BC at night was much

293   stronger than that in the daytime. The main reason will be discussed in Section 3.3.

3.1.3 Diurnal variations of BC core diameter and coating thickness

295   BC core diameter (D_c) can be obtained if knowing single particle BC mass and

296   assuming that core is spherical and BC density is 1.8 g/cm^3. The corresponding

297   coating thickness is $(D_p - D_c)/2$ (Gong et al., 2016). Diurnal variations in average BC

298   core diameter and coating thickness at different GFs are displayed in Fig. 5(a) and Fig.

299   5(b), respectively. For a certain BC particle size, a larger core size and a thinner

300   coating thickness corresponded to BC particles with lower hygroscopicity (e.g.

301   GF=1.0). When BC particles became more hygroscopic (i.e. GF increases), the

302   coating thickness increased.

303   It's interesting to note that the core sizes for the hygroscopic mode BC particles

304   increased during nighttime (21:00 to 6:00) while coating thickness decreased (since

305   the entire electron mobility diameter was fixed). This observation suggests that the

306   coating material on BC particle might be different between daytime and nighttime. To

307   achieve the same GF, a thicker coating thickness is required for the less hygroscopic

308   coating materials, as the hygroscopicity of BC core is always constant (GF = 1.0).

3.2 BC-containing particle types identified by SPAMS

310   The mixing state and aging degree of BC-containing particles have been studied

311   using a SPAMS. Noticeably, the particles size range for the SPAMS is from 200 to

312   2000 nm. The detection efficiency drops rapidly below 400 nm and above 1200 nm

313   (Li et al., 2011). However, most pure BC particles are smaller than 200 nm (Kondo et

314   al., 2006), which is close to the lower size limit for the SPAMS and can only be

315   detected at a low efficiency. Based on SPAMS mass spectra patterns, BC particles

316   were classified into five types: EC, NaKEC, ECOC, KEC and Others. Their relative

317   contributions are shown in Table 1. The average mass spectra for each particle type

318   are shown in Fig. S2.

319   Pure EC particles only presented BC fragment ions (C_n^+ and C_n^-) in both positive

320   and negative ion mass spectra. There were low signals of secondary species, such as

321   sulfate or nitrate, indicating that pure EC had not gone through significant aging in the

322   atmosphere, thus EC type were freshly emitted BC particles.

323   NaKEC particles exhibited strong signals for BC fragment ions in both positive

324   and negative mass spectra, in addition, potassium ($^{+39}K^+$) and sodium ($^{+23}Na^+$) in

325   positive ion mass spectra and nitrate ($^{-46}NO_2^-$ and $^{-62}NO_3^-$) and sulfate ($^{-97}HSO_4^-$) in the

326   negative ion mass spectra also exhibited. Hydrocarbon-like organic aerosol (HOA) is

327   dominated by alkyl fragment signatures, the $C_nH_{2n+1}^+$ (m/z= 29, 43, 57) and $C_nH_{2n-1}^+$

328   (m/z= 27, 41, 55) ions. The time series of HOA correlated well with those of NO_2 and

329   CO, two tracers of vehicle emissions (Fig. S3(a)). The diurnal pattern of HOA ion

330   intensity further suggests the association of HOA with traffic activities, as it showed

331   two obvious peaks during the morning and evening rush hours (Li et al., 2017). HOA

332   as a tracer of traffic emission correlated reasonably well with the NaKEC particles

333   number (R^2=0.560), as shown in Fig. S3(b).

334   The ECOC type particles internally mixed with many organic carbon (OC)

335   signals, including $^{+37}C_3H$, $^{+43}CH_3CO^+$, $^{+50}C_4H_2^+$, $^{+51}C_4H^+$, $^{+61}CH_3C(OH)=OH^+$,

336    $^{+62}(CH_3)_2NHOH^+$, as well as $^{+23}Na^+$ and BC fragment ions (C_n^+). The presence of a

337   high signal intensity for sulfate ($^{-97}HSO_4^-$) and a relatively low signal intensity for

338   nitrate ($^{-46}NO_3^-$, $^{-62}NO_3^-$) suggests that they were aged BC particles. BC particles with

339   various intensities of OC, nitrate and sulfate were commonly detected in ambient

340 measurements by ATOFMS (Moffet et al., 2008; Ault et al., 2009) (Dall' Osto and

341 Harrison, 2006) and were also assigned to aged traffic emissions (Healy et al., 2012).

342  KEC particles were characterized by an intense $^{+39}K^+$ signal in the positive ion

343 mass spectra and strong signals for $^{-26}CN^-$ and $^{-42}CNO^-$ in the negative ion mass

344 spectra. Significant intensities of ion fragments of levoglucosan, such as $^{-71}C_3H_3O_2^-$

345 and $^{-73}C_3H_5O_2^-$, were also observed. Typical BC fragments C_n^- appeared in the negative

346 ion mass spectra. Similar to ECOC type, the presence of a high signal intensity of

347 $^{-97}HSO_4^-$, $^{-46}NO_2^-$ and $^{-62}NO_3^-$ signals indicates significant particle aging in the

348 atmosphere (Leskinen et al., 2007; Reid et al., 2005). These characteristics suggest

349 that their sources are either biomass burning or coal combustion or both (Andreae,

350 1983; Soto-Garcia et al., 2011; Wang et al., 2013; Gong et al., 2016). Particles with

351 similar mass spectral patterns were previously observed in several urban field studies

352 are also assigned to the sources of combustion of biomass or coal (Moffet et al., 2008;

353 Healy et al., 2012; Bi et al., 2011; Wang et al., 2013; Gong et al., 2016).

354  "Others" particle type was not grouped to any of the previous four types; and it

355 accounts for only 8.5% in total BC particle number concentration. The average mass

356 spectra of this particle type are displayed in Fig. S2 (e). However, it is not the focus of

357 this study.

358  The relative fractions of aerosol types as a function of particle size were plotted

359 in Fig. S4. Generally, the number fraction for each particle type is highly dependent

360 on particle size. Sharp changes in BC particle mixing states has been found between

361 the size ranges of 200 nm ~ 400 nm and 400nm ~ 800nm. EC and NaKEC types are

362 the major fraction types in the 200 nm ~ 400 nm size range. In contrast, the larger size

363 range (400 nm ~ 800 nm) was dominated by ECOC and KEC types. For the sake of

364 the convenience for discussion, we separate particles to two groups based on their d_{va},

365 namely $G_{200-400}$ (200 nm< d_{va} <400 nm) and $G_{400-800}$ (400 nm< d_{va} <800 nm). In this

366 work, d_{va} = 150 nm (d_m = 120 nm) was out of the SPAMS detection range, while d_{va} =

367   312 nm (d_m = 240 nm) and d_{va} = 468 nm (d_m = 360 nm) was falling in the range of

368     $G_{200-400}$ and $G_{400-800}$, respectively.

369   The diurnal variations of number fraction of each particle type in $G_{200-400}$ were

370   calculated and shown in Fig. 6(a). It is found that number fraction of the EC and

371   NaKEC types displayed pronounced diurnal patterns with two major peaks in the

372   early morning (6:00 ~ 9:00) and in the evening (18:00 ~ 21:00), which possibly

373   related to traffic. From the hygroscopicity measurement (D_0 = 240 and 360 nm in Fig.

374   4(a)), the elevated BC particle number concentration at GF=1.0 during these two

375   time-frames suggests that the elevated concentrations of hydrophobic BC particles

376   aerosol were probably associated with EC and NaKEC types, which are produced

377   from traffic sources.

378   A different pattern has been observed for $G_{400-800}$ (shown in Fig. 6(b)). The

379   ECOC and KEC types accounted for the major number fractions in the 400 nm ~ 800

380   nm range. The diurnal variations of these two particle types share a similar trend,

381   while other two types (EC and NaKEC) showed no significant variation. The EC and

382   NaKEC types only attributed to small proportions of $G_{400-800}$ particles. Interestingly,

383   the number fraction of ECOC in $G_{400-800}$ also showed two major peaks in the morning

384   and evening, suggesting that ECOC was aged BC particles from traffic emissions. The

385   KEC peak in the evening was much more pronounced than that in the morning, and

386   this might be due to biomass burning which is still widely used by domestic cooking

387   (in the evening) in the countryside around Shanghai city. These BB aerosols were

388   then transport to the sampling site.

389   **3.3 The relations between the mixing state and hygroscopicity of BC particles**

390   To elucidate the relation between mixing state and hygroscopicity of BC

391   particles, the detailed chemical composition and mixing state information from the

392   EC/OC, MARGA and SPAMS was compared to the HTDMA-SP2 hygroscopicity

393   measurements. As discussed in Section 3.1, we found that the BC core sizes for the

394   hygroscopic mode particles increased during nighttime (21:00 ~ 6:00) while coating

395   thickness decreased, indicating the BC particle coating compositions were different

396   between daytime and nighttime. The major secondary aerosol coating materials in

397   polluted boundary layer could be secondary organic carbon (SOC), sulfate and nitrate.

398   Therefore, the diurnal trends of these species have been investigated and compared to

399   BC particles' hygroscopicity.

400   3.3.1 Major secondary ionic species

401   The dominant ionic species in urban aerosols in Shanghai are sulfate, nitrate and

402   ammonium (Ye et al., 2013). To study the chemical composition dependence on

403   hygroscopicity, mass concentrations of SO_4^{2-}, NO_3^- and NH_4^+ were measured by a

404   MARGA during this field study. As shown in Fig. 7(c), the average sulfate

405   concentration varied in a small range from ~ 4.8 to 6.1 µg/m^3. Its concentration in the

406   daytime was only slightly higher than that of nighttime. The average mass

407   concentration of NO_3^- varied between 1.1 µg/m^3 and 4.4 µg/m^3 with an average of 2.3

408   µg/m^3. Similar to our previous study (Wang et al., 2016a), the nitrate concentrations

409   at night were clearly elevated (Fig. 7(d)). The relative peak area (RPA) of NO_3^- in

410   BC particles measured by SPAMS is also consistent with the MARGA measurement

411   (Fig. 7(d)). During the nighttime in summer, lower temperature, higher relative

412   humidity and high concentration of NO_3 (N_2O_5) favor the formation of nitrate in

413   particle phase (Wang et al., 2009; Wang et al., 2016a).

414   3.3.2 Elevated SOC concentrations in the daytime

415   Photochemical reactions are a major formation pathway of SOC (Kroll and

416   Seinfeld, 2008; Zhang et al., 2018). Odd oxygen ($O_x = O_3 + NO_2$) was often used as

417   an indicator of photochemical oxidant concentration in the atmosphere (Herndon et al.,

418   2008; Hu et al., 2016; Wood et al., 2010). The diurnal variations of SOC and O_x mass

419   concentrations in one-hour resolution were plotted in Fig. 7. In this work, average

420   SOC and O_x varied between 1.8 µgC/m^3 and 8.8 µgC/m^3, and 58 µg/m^3 and 214

421   µg/m^3, respectively. The correlation coefficient (R) between SOC and O_x was 0.772

422   (shown in Fig. S5), indicating that the SOC formation was associated with the

423   photochemical oxidant concentration during this study.

424   Single particle mass spectrometry was also used to further investigate the mixing

425   state and possible formation pathways of SOC. The relative peak area of

426   +43[CH_3CO^+/$CHNO^+$] during the daytime is a tracer of SOC formation (Qin et al.,

427   2012; Zhang et al., 2014; Zhang et al., 2018). Time-series of hourly-averaged relative

428   peak areas of m/z +43 in ECOC type was shown in Fig. 8. Overall, the m/z +43 curve

429   peaked in the afternoon, which was consistent with the trend of O_x. This result

430   indicates that SOC (m/z=+43) produced by photochemical reactions condensed on BC

431   particles. The average ECOC particle size verse time is also shown in Fig. 8. It peaked

432   between 13:00 to 15:00 in the afternoon. Since the concentration of sulfate in the

433   daytime was only slightly higher than that of nighttime (Fig. 7(c)), the increase of

434   ECOC particle size was mainly caused by the condensation of SOC rather than

435   secondary inorganic species. Therefore, in the afternoon, the intense photochemical

436   processes resulted in BC particles coated with more organic materials, leading to a

437   thicker coating thickness.

438   **3.3.3 Hygroscopicity and mixing state (coating material)**

439   As discussed above, the chemical composition measurement clearly shows BC

440   particles were coated more SOC in the daytime and more nitrate in the nighttime.

441   Sulfate concentration did not change much between daytime and nighttime.

442   Meanwhile, at a given GF, the coating for hygroscopic mode BC particles was thicker

443   in the daytime and thinner in the nighttime. The water uptake ability of nitrate is much

444   stronger than secondary organics. Thus, compared to SOC, less nitrate coating is

445   needed for a given hygroscopicity or GF.

446   To better understand this finding, we estimated volumes of different coating

447   materials required for a BC particle with a given hygroscopicity using the

448   Zdanovskii-Stokes-Robinson (ZSR) mixing rule (Stokes and Robinson, 1966),

449
$$\mathrm{GF}_{ZSR}(\mathrm{RH}, D_p) = \left(\sum_i \mathrm{GF}_i(\mathrm{RH}, D_p)^3 \varepsilon_i \right)^{1/3} \qquad (2)$$

450   The ε_i is the volume fractions of rBC, nitrate, sulfate or organic coating in BC

451   particles. For simplicity, we assume BC is covered by mixture containing either

452     $SOC/(NH_4)_2SO_4$ or $(NH_4)_2SO_4/NH_4NO_3$, representing the mixing state of BC in

453   daytime and nighttime respectively. The GF for SOC is set to be 1.2, since Sjogren et

454   al. reported a uniform growth factor GF_{SOA}=1.2 (RH=90%) according to the ZSR

455   modelling results and field measurements (Sjogren et al., 2008). This value is at the

456   high end of previous measured SOA hygroscopicity range, thereby representing

457   highly aged and oxidized of SOA (Varutbangkul et al., 2006; Baltensperger et al.,

458   2005). The GFs of pure black carbon, $(NH_4)_2SO_4$ and NH_4NO_3 aerosol with a dry size

459   of 163 nm at RH=90% are calculated using the Aerosol Diameter-Dependent

460   Equilibrium Model (ADDEM) model. Their values are 1.0, 1.7 and 1.8 respectively

461   (Topping et al., 2005a, b).

462   For a coated BC particle with a dry diameter of 163 nm and a GF of 1.4, the

463   following relations would hold for $SOC/(NH_4)_2SO_4$ coating (eq. 3) and

464     $(NH_4)_2SO_4/NH_4NO_3$ coating (eq. 4):

465
$$1.4 = \sqrt[3]{\varepsilon_{BC} \times \mathrm{GF}_{BC}^3 + \varepsilon_{SOC} \times \mathrm{GF}_{SOC}^3 + \varepsilon_{(NH_4)_2SO_4} \times \mathrm{GF}_{(NH_4)_2SO_4}^3} \qquad (3)$$

466
$$1.4 = \sqrt[3]{\varepsilon_{BC}' \times \mathrm{GF}_{BC}^3 + \varepsilon_{NH_4NO_3} \times \mathrm{GF}_{NH_4NO_3}^3 + \varepsilon_{(NH_4)_2SO_4} \times \mathrm{GF}_{(NH_4)_2SO_4}^3} \qquad (4)$$

467   ε_{BC} and ε_{BC}', representing the volume fractions of BC core in two mixing states,

468   are given by $\varepsilon_{BC} = 1 - \varepsilon_{SOC} - \varepsilon_{(NH_4)_2SO_4}$ and $\varepsilon'_{BC} = 1 - \varepsilon_{NH_4NO_3} - \varepsilon_{(NH_4)_2SO_4}$, respectively.

469   Here, we assume $\varepsilon_{(NH_4)_2SO_4}$ is constant in both mixing states.

470   Combining equations above, the ratio of volume fraction of SOC to NH₄NO₃ is

471    $$\frac{\varepsilon_{SOC}}{\varepsilon_{NH_4NO_3}} = 6.6 \qquad (5)$$

472   This calculation shows that higher volume fraction of SOC/(NH₄)₂SO₄ is needed for a

473   BC particle to achieve the same GF as the one covered by (NH₄)₂SO₄/NH₄NO₃.

474   This result confirms that different atmospheric aging pathways lead to changes in

475   aerosol mixing state with distinct hygroscopicities: During nighttime with low

476   temperature and high RH, formation or condensation of nitrates on BC particles

477   enhanced the hygroscopicity of BC particles and resulted in the thinner coating BC

478   particles in the hygroscopic mode for each selected size. During daytime,

479   condensation of photo-chemically generated SOC on BC particles was associated to

480   the thicker coating BC particles with less enhancement of hygroscopicity. The sulfate

481   coating could enhance hygroscopicity of BC particles. However, unlike nitrate and

482   SOC, its formation did not show a significant difference between day and night.

4 Conclusions

484   In this study, a HTDMA+SP2 system along with SPAMS were used to measure

485   BC particles' hygroscopic properties in Shanghai during 2017 summer. Three

486   hygroscopic modes, namely the hydrophobic mode, transition mode and hydrophilic

487   mode with GF at 1.0, 1.2 and 1.4, respectively, were selected to study the diurnal

488   variations in BC core and coating thickness as a function of time.

489   Our results reveal that the hygroscopicity of BC particle is determined by the

490   coating layer thickness and materials, both of which are affected by atmospheric

491   aging processes. For a specific BC particle size, a thin coating layer corresponded to

492   freshly emitted BC particles with low hygroscopicity (e.g. GF=1.0). When BC

493   particles became more hygroscopic (i.e. GF increases), the coating thickness

494   increased. High yielding of particulate nitrate during nighttime was observed, and

495   nitrate coating greatly enhanced the hygroscopicity of BC particles. During daytime,

496   strong SOC formation from photochemical oxidation played an important role in the

497   evolution of the BC mixing state. A thinner layer of nitrate coating could convert

498   fresh BC particles to aged hygroscopic ones while a thicker coating layer of SOC and

499   sulfate was required to reach the same overall hygroscopicity.

500   This study shows that atmospheric aging processes in a polluted city area play

501   critical roles in the fast changing of aerosol mixing state during summer time. Time

502   resolved information on particle hygroscopicity is necessary to evaluate the aging

503   process, wet removal as well as climate effects of BC aerosols.

504

505   **Acknowledgements**

506   This work was supported by the National Natural Science Foundation of China (Nos.

507   91544224, 41775150, 21507010).

508

509

510

511

512

References

Andreae, M. O.: Soot carbon and excess fine potassium: Long-range transport of combustion-derived aerosols, Science, 220, 1148–1151, https://doi.org/10.1126/science.220.4602.1148, 1983.

Ault, A. P., Moore, M. J., Furutani, H., and Prather, K. A.: Impact of emissions from the Los Angeles port region on San Diego air quality during regional transport events, Environ. Sci. Technol., 43, 3500–3506, https://doi.org/10.1021/es8018918, 2009.

Baltensperger, U., Kalberer, M., Dommen, J., Paulsen, D., Alfarra, M. R., Coe, H., Fisseha, R., Gascho, A., Gysel, M., and Nyeki, S.: Secondary organic aerosols from anthropogenic and biogenic precursors, Faraday Discussions, 130, 265–278, https://doi.org/ 10.1039/b417367h, 2005.

Bi, X., Zhang, G., Li, L., Wang, X., Li, M., Sheng, G., Fu, J., and Zhou, Z.: Mixing state of biomass burning particles by single particle aerosol mass spectrometer in the urban area of PRD, China, Atmos. Environ., 45, 3447–3453, https://doi.org/10.1016/j.atmosenv.2011.03.034, 2011.

Bond, T. C., Doherty, S. J., Fahey, D., Forster, P., Berntsen, T., DeAngelo, B., Flanner, M., Ghan, S., Kärcher, B., and Koch, D.: Bounding the role of black carbon in the climate system: A scientific assessment, J. Geophys. Res.-Atmos., 118, 5380–5552, https://doi.org/10.1002/jgrd.50171, 2013.

Cao, J.-J., Zhu, C.-S., Tie, X.-X., Geng, F.-H., Xu, H.-M., Ho, S., Wang, G.-H., Han, Y.-M., and Ho, K.-F.: Characteristics and sources of carbonaceous aerosols from Shanghai, China, Atmos. Chem. Phys., 13, 803–817, https://doi.org/10.5194/acp-13-803-2013, 2013.

537   Change, I. P. o. C.: Climate change 2014: mitigation of climate change, Cambridge
538   University Press, 2015.

539   Chen, J., Zhao, C., Ma, N., Liu, P., Göbel, T., Hallbauer, E., Deng, Z., Ran, L., Xu,
540   W., and Liang, Z.: A parameterization of low visibilities for hazy days in the
541   North China Plain, Atmos. Chem. Phys., 12, 4935–4950,
542   https://doi.org/10.5194/acp-12-4935-2012, 2012.

543   Chirico, R., DeCarlo, P., Heringa, M., Tritscher, T., Richter, R., Prévôt, A., Dommen,
544   J., Weingartner, E., Wehrle, G., and Gysel, M.: Impact of aftertreatment devices
545   on primary emissions and secondary organic aerosol formation potential from
546   in-use diesel vehicles: results from smog chamber experiments, Atmos. Chem.
547   Phys., 10, 11545–11563, https://doi.org/10.5194/acp-10-11545-2010, 2010.

548   Chou, C.-K., Lee, C., Cheng, M., Yuan, C., Chen, S., Wu, Y., Hsu, W., Lung, S., Hsu,
549   S., and Lin, C.: Seasonal variation and spatial distribution of carbonaceous
550   aerosols in Taiwan, Atmos. Chem. Phys., 10, 9563–9578,
551   https://doi.org/10.5194/acp-10-9563-2010, 2010.

552   Dall'Osto, M., and Harrison, R. M.: Chemical characterisation of single airborne
553   particles in Athens (Greece) by ATOFMS, Atmos. Environ., 40, 7614–7631,
554   https://doi.org/10.1016/j.atmosenv.2006.06.053, 2006.

555   Du, H., Kong, L., Cheng, T., Chen, J., Yang, X., Zhang, R., Han, Z., Yan, Z., and Ma,
556   Y.: Insights into ammonium particle-to-gas conversion: non-sulfate ammonium
557   coupling with nitrate and chloride, Aerosol Air Qual. Res., 10, 589–595,
558   https://doi.org/ 10.4209/aaqr.2010.04.0034, 2010.

559   Gong, X., Zhang, C., Chen, H., Nizkorodov, S. A., Chen, J., and Yang, X.: Size
560   distribution and mixing state of black carbon particles during a heavy air

561   pollution episode in Shanghai, Atmos. Chem. Phys., 16, 5399–5411,

562   https://doi.org/10.5194/acp-16-5399-2016, 2016.

563 Healy, R. M., Sciare, J., Poulain, L., Kamili, K., Merkel, M., Müller, T.,

564   Wiedensohler, A., Eckhardt, S., Stohl, A., and Sarda-Estève, R.: Sources and

565   mixing state of size-resolved elemental carbon particles in a European megacity:

566   Paris,   Atmos.   Chem.   Phys.,   12,   1681–1700,

567   https://doi.org/10.5194/acp-12-1681-2012, 2012.

568 Herich, H., Kammermann, L., Gysel, M., Weingartner, E., Baltensperger, U.,

569   Lohmann, U., and Cziczo, D. J.: In situ determination of atmospheric aerosol

570   composition as a function of hygroscopic growth, J. Geophys. Res.-Atmos., 113,

571   D16213, https://doi.org/10.1029/2008JD009954, 2008.

572 Heringa, M., DeCarlo, P., Chirico, R., Tritscher, T., Dommen, J., Weingartner, E.,

573   Richter, R., Wehrle, G., Prévôt, A., and Baltensperger, U.: Investigations of

574   primary and secondary particulate matter of different wood combustion

575   appliances with a high-resolution time-of-flight aerosol mass spectrometer,

576   Atmos. Chem. Phys., 11, 5945–5957, https://doi.org/10.5194/acp-11-5945-2011,

577   2011.

578 Herndon, S. C., Onasch, T. B., Wood, E. C., Kroll, J. H., Canagaratna, M. R., Jayne, J.

579   T., Zavala, M. A., Knighton, W. B., Mazzoleni, C., and Dubey, M. K.:

580   Correlation of secondary organic aerosol with odd oxygen in Mexico City,

581   Geophys. Res. Lett., 35, L15804, https://doi.org/10.1029/2008GL034058, 2008.

582 Hu, W., Hu, M., Hu, W., Jimenez, J. L., Yuan, B., Chen, W., Wang, M., Wu, Y.,

583   Chen, C., and Wang, Z.: Chemical composition, sources, and aging process of

584   submicron aerosols in Beijing: Contrast between summer and winter, J. Geophys.

585   Res.-Atmos., 121, 1955–1977, https://doi.org/10.1002/2015JD024020, 2016.

586 Huang, X.-F., Sun, T.-L., Zeng, L.-W., Yu, G.-H., and Luan, S.-J.: Black carbon
587   aerosol characterization in a coastal city in South China using a single particle
588   soot photometer, Atmos. Environ., 51, 21–28,
589   https://doi.org/10.1016/j.atmosenv.2012.01.056, 2012.

590 Huang, Y., Li, L., Li, J., Wang, X., Chen, H., Chen, J., Yang, X., Gross, D., Wang, H.,
591   and Qiao, L.: A case study of the highly time-resolved evolution of aerosol
592   chemical and optical properties in urban Shanghai, China, Atmos. Chem. Phys.,
593   13, 3931–3944, https://doi.org/10.5194/acp-13-3931-2013, 2013.

594 Kondo, Y., Komazaki, Y., Miyazaki, Y., Moteki, N., Takegawa, N., Kodama, D.,
595   Deguchi, S., Nogami, M., Fukuda, M., and Miyakawa, T.: Temporal variations
596   of elemental carbon in Tokyo, J. Geophys. Res.-Atmos., 111, D12205,
597   https://doi.org/10.1029/2005JD006257, 2006.

598 Kondo, Y.: Effects of black carbon on climate: Advances in measurement and
599   modeling, Monographs on Environment, Environ. Earth Planets, 3, 1–85,
600   https://doi.org/10.5047/meep.2015.00301.0001, 2015.

601 Kroll, J. H., and Seinfeld, J. H.: Chemistry of secondary organic aerosol: Formation
602   and evolution of low-volatility organics in the atmosphere, Atmos. Environ., 42,
603   3593–3624, https://doi.org/10.1016/j.atmosenv.2008.01.003, 2008.

604 Löndahl, J., Massling, A., Pagels, J., Swietlicki, E., Vaclavik, E., and Loft, S.:
605   Size-resolved respiratory-tract deposition of fine and ultrafine hydrophobic and
606   hygroscopic aerosol particles during rest and exercise, Inhal. Toxicol., 19, 109–
607   116, https://doi.org/10.1080/08958370601051677, 2007.

608 Laborde, M., Crippa, M., Tritscher, T., Jurányi, Z., Decarlo, P., Temime-Roussel, B.,
609   Marchand, N., Eckhardt, S., Stohl, A., and Baltensperger, U.: Black carbon

610   physical properties and mixing state in the European megacity Paris, Atmos.

611   Chem. Phys., 13, 5831–5856, https://doi.org/10.5194/acp-13-5831-2013, 2013.

612   Leskinen, A. P., Jokiniemi, J. K., and Lehtinen, K. E.: Characterization of aging wood

613   chip combustion aerosol in an environmental chamber, Atmos. Environ., 41,

614   3713–3721, https://doi.org/10.1016/j.atmosenv.2006.12.016, 2007.

615   Li, H., Zhang, Q., Zhang, Q., Chen, C., Wang, L., Wei, Z., Zhou, S., Parworth, C.,

616   Zheng, B., and Canonaco, F.: Wintertime aerosol chemistry and haze evolution

617   in an extremely polluted city of the North China Plain: significant contribution

618   from coal and biomass combustion, Atmos. Chem. Phys., 17, 4751–4768,

619   https://doi.org/10.5194/acp-17-4751-2017, 2017.

620   Li, L., Huang, Z., Dong, J., Li, M., Gao, W., Nian, H., Fu, Z., Zhang, G., Bi, X., and

621   Cheng, P.: Real time bipolar time-of-flight mass spectrometer for analyzing

622   single aerosol particles, Int. J. Mass Spectrom., 303, 118–124,

623   https://doi.org/10.1016/j.ijms.2011.01.017, 2011.

624   Liu, D., Allan, J., Whitehead, J., Young, D., Flynn, M., Coe, H., McFiggans, G.,

625   Fleming, Z. L., and Bandy, B.: Ambient black carbon particle hygroscopic

626   properties controlled by mixing state and composition, Atmos. Chem. Phys., 13,

627   2015–2029, https://doi.org/10.5194/acp-13-2015-2013, 2013.

628   Matsui, H., Koike, M., Kondo, Y., Moteki, N., Fast, J. D., and Zaveri, R. A.:

629   Development and validation of a black carbon mixing state resolved three‐

630   dimensional model: Aging processes and radiative impact, J. Geophys.

631   Res.-Atmos., 118, 2304–2326, https://doi.org/10.1029/2012JD018446, 2013.

632   McMeeking, G., Good, N., Petters, M., McFiggans, G., and Coe, H.: Influences on the

633   fraction of hydrophobic and hydrophilic black carbon in the atmosphere, Atmos.

634   Chem. Phys., 11, 5099–5112, https://doi.org/10.5194/acp-11-5099-2011, 2011.

635   Moffet, R., Foy, B. d., Molina, L. a., Molina, M., and Prather, K.: Measurement of
636   ambient aerosols in northern Mexico City by single particle mass spectrometry,
637   Atmos. Chem. Phys., 8, 4499–4516, https://doi.org/10.5194/acp-8-4499-2008,
638   2008.

639   Mogili, P. K., Kleiber, P. D., Young, M. A., and Grassian, V. H.: N_2O_5 hydrolysis on
640   the components of mineral dust and sea salt aerosol: Comparison study in an
641   environmental aerosol reaction chamber, Atmos. Environ., 40, 7401–7408,
642   https://doi.org/10.1016/j.atmosenv.2006.06.048, 2006.

643   Notario, A., Bravo, I., Adame, J. A., Díaz-de-Mera, Y., Aranda, A., Rodríguez, A.,
644   and Rodríguez, D.: Analysis of NO, NO_2, NO_x, O_3 and oxidant ($O_x = O_3 + NO_2$)
645   levels measured in a metropolitan area in the southwest of Iberian Peninsula,
646   Atmos. Res., 104, 217–226, https://doi.org/10.1016/j.atmosres.2011.10.008,
647   2012.

648   Pratt, K., Murphy, S., Subramanian, R., DeMott, P., Kok, G., Campos, T., Rogers, D.,
649   Prenni, A., Heymsfield, A., and Seinfeld, J.: Flight-based chemical
650   characterization of biomass burning aerosols within two prescribed burn smoke
651   plumes, Atmos. Chem. Phys., 11, 12549–12565,
652   https://doi.org/10.5194/acp-11-12549-2011, 2011.

653   Qin, X., Pratt, K. A., Shields, L. G., Toner, S. M., and Prather, K. A.: Seasonal
654   comparisons of single-particle chemical mixing state in Riverside, CA, Atmos.
655   Environ., 59, 587–596, https://doi.org/10.1016/j.atmosenv.2012.05.032, 2012.

656   Reid, J., Koppmann, R., Eck, T., and Eleuterio, D.: A review of biomass burning
657   emissions part II: intensive physical properties of biomass burning particles,
658   Atmos. Chem. Phys., 5, 799–825, https://doi.org/10.5194/acp-5-799-2005, 2005.

659 Schneider, J., Hock, N., Weimer, S., Borrmann, S., Kirchner, U., Vogt, R., and Scheer,
660   V.: Nucleation particles in diesel exhaust: Composition inferred from in situ
661   mass spectrometric analysis, Environ. Sci. Technol., 39, 6153–6161,
662   https://doi.org/10.1021/es049427m, 2005.

663 Shiraiwa, M., Kondo, Y., Moteki, N., Takegawa, N., Miyazaki, Y., and Blake, D.:
664   Evolution of mixing state of black carbon in polluted air from Tokyo, Geophys.
665   Res. Lett., 34, L16803, https://doi.org/10.1029/2007GL029819, 2007.

666 Sjogren, S., Gysel, M., Weingartner, E., Alfarra, M., Duplissy, J., Cozic, J., Crosier, J.,
667   Coe, H., and Baltensperger, U.: Hygroscopicity of the submicrometer aerosol at
668   the high-alpine site Jungfraujoch, 3580 m asl, Switzerland, Atmos. Chem. Phys.,
669   8, 5715–5729, https://doi.org/10.5194/acp-8-5715-2008, 2008.

670 Slowik, J. G., Stainken, K., Davidovits, P., Williams, L., Jayne, J., Kolb, C., Worsnop,
671   D. R., Rudich, Y., DeCarlo, P. F., and Jimenez, J. L.: Particle morphology and
672   density characterization by combined mobility and aerodynamic diameter
673   measurements. Part 2: Application to combustion-generated soot aerosols as a
674   function of fuel equivalence ratio, Aerosol Sci. Tech., 38, 1206–1222,
675   https://doi.org/10.1080/027868290903916, 2004.

676 Song, X.-H., Hopke, P. K., Fergenson, D. P., and Prather, K. A.: Classification of
677   single particles analyzed by ATOFMS using an artificial neural network,
678   ART-2A, Anal. Chem., 71, 860–865, https://doi.org/ 10.1021/ac9809682, 1999.

679 Soto-Garcia, L. L., Andreae, M. O., Andreae, T. W., Artaxo, P., Maenhaut, W.,
680   Kirchstetter, T., Novakov, T., Chow, J. C., and Mayol-Bracero, O. L.: Evaluation
681   of the carbon content of aerosols from the burning of biomass in the Brazilian
682   Amazon using thermal, optical and thermal-optical analysis methods, Atmos.
683   Chem. Phys., 11, 4425–4444, https://doi.org/10.5194/acp-11-4425-2011, 2011.

684   Spencer, M. T., Shields, L. G., and Prather, K. A.: Simultaneous measurement of the

685   effective density and chemical composition of ambient aerosol particles, Environ.

686   Sci. Technol., 41, 1303–1309, https://doi.org/10.1021/es061425+, 2007.

687   Stokes, R., and Robinson, R.: Interactions in aqueous nonelectrolyte solutions. I.

688   Solute-solvent   equilibria,   J.   Phys.   Chem.,   70,   2126–2131,

689   https://doi.org/10.1021/j100879a010, 1966.

690   Swietlicki, E., HANSSON, H. C., Hämeri, K., Svenningsson, B., Massling, A.,

691   McFiggans, G., McMurry, P., Petäjä, T., Tunved, P., and Gysel, M.:

692   Hygroscopic properties of submicrometer atmospheric aerosol particles

693   measured with H‑TDMA instruments in various environments–A review,

694   Tellus B, 60, 432–469, https://doi.org/10.1111/j.1600-0889.2008.00350.x, 2008.

695   Topping, D., McFiggans, G., and Coe, H.: A curved multi-component aerosol

696   hygroscopicity model framework: Part 2–Including organic compounds, Atmos.

697   Chem. Phys., 5, 1223–1242, https://doi.org/10.5194/acp-5-1223-2005, 2005a.

698   Topping, D., McFiggans, G., and Coe, H.: A curved multi-component aerosol

699   hygroscopicity model framework: Part 1–Inorganic compounds, Atmos. Chem.

700   Phys., 5, 1205–1222, https://doi.org/10.5194/acp-5-1205-2005, 2005b.

701   Varutbangkul, V., Brechtel, F., Bahreini, R., Ng, N., Keywood, M., Kroll, J., Flagan,

702   R., Seinfeld, J., Lee, A., and Goldstein, A.: Hygroscopicity of secondary organic

703   aerosols formed by oxidation of cycloalkenes, monoterpenes, sesquiterpenes, and

704   related   compounds,   Atmos.   Chem.   Phys.,   6,   2367–2388,

705   https://doi.org/10.5194/acp-6-2367-2006, 2006.

706   Wang, D., Zhou, B., Fu, Q., Zhao, Q., Zhang, Q., Chen, J., Yang, X., Duan, Y., and Li,

707   J.: Intense secondary aerosol formation due to strong atmospheric photochemical

708   reactions in summer: observations at a rural site in eastern Yangtze River Delta

709   of   China,   Sci.   Total   Environ.,   571,   1454–1466,

710   https://doi.org/10.1016/j.scitotenv.2016.06.212, 2016a.

711   Wang, Q., Huang, R.-J., Zhao, Z., Zhang, N., Wang, Y., Ni, H., Tie, X., Han, Y.,

712   Zhuang, M., and Wang, M.: Size distribution and mixing state of refractory black

713   carbon aerosol from a coastal city in South China, Atmos. Res., 181, 163–171,

714   https://doi.org/10.1016/j.atmosres.2016.06.022, 2016b.

715   Wang, X., Zhang, Y., Chen, H., Yang, X., Chen, J., and Geng, F.: Particulate nitrate

716   formation in a highly polluted urban area: a case study by single-particle mass

717   spectrometry   in   Shanghai,   Environ.   Sci.   Technol.,   43,   3061–3066,

718   https://doi.org/10.1021/es8020155, 2009.

719   Wang, X., Williams, B. J., Wang, X., Tang, Y., Huang, Y., Kong, L., Yang, X., and

720   Biswas, P.: Characterization of organic aerosol produced during pulverized coal

721   combustion in a drop tube furnace, Atmos. Chem. Phys., 13, 10919–10932,

722   https://doi.org/10.5194/acp-13-10919-2013, 2013.

723   Wang, X., Ye, X., Chen, H., Chen, J., Yang, X., and Gross, D. S.: Online

724   hygroscopicity and chemical measurement of urban aerosol in Shanghai, China,

725   Atmos. Environ., 95, 318–326, https://doi.org/10.1016/j.atmosenv.2014.06.051,

726   2014.

727   Wood, E., Canagaratna, M., Herndon, S., Onasch, T., Kolb, C., Worsnop, D., Kroll, J.,

728   Knighton, W., Seila, R., and Zavala, M.: Investigation of the correlation between

729   odd oxygen and secondary organic aerosol in Mexico City and Houston, Atmos.

730   Chem. Phys., 10, 8947–8968, https://doi.org/10.5194/acp-10-8947-2010, 2010.

731   Xue, J., Li, Y., Wang, X., Durbin, T.D., Johnson, K.C., Karavalakis, G., Asa-Awuku,

732   A., Villela, M., Quiros, D., Hu, S. and Huai, T.: Comparison of vehicle exhaust

733   particle size distributions measured by SMPS and EEPS during steady-state

734   conditions, Aerosol Sci. Tech., 49, 984–996, https://doi:
735   10.1080/02786826.2015.1088146, 2015.

736   Ye, X., Chen, T., Hu, D., Yang, X., Chen, J., Zhang, R., Khakuziv, A. F., and Wang,
737   L.: A multifunctional HTDMA system with a robust temperature control, Adv.
738   Atmos. Sci., 26, 1235–1240, https://doi.org/10.1007/s00376-009-8134-3, 2009.

739   Ye, X., Tang, C., Yin, Z., Chen, J., Ma, Z., Kong, L., Yang, X., Gao, W., and Geng,
740   F.: Hygroscopic growth of urban aerosol particles during the 2009
741   Mirage-Shanghai Campaign, Atmos. Environ., 64, 263–269,
742   https://doi.org/10.1016/j.atmosenv.2012.09.064, 2013.

743   Zhai, J., Lu, X., Li, L., Zhang, Q., Zhang, C., Chen, H., Yang, X., and Chen, J.:
744   Size-resolved chemical composition, effective density, and optical properties of
745   biomass burning particles, Atmos. Chem. Phys., 17, 7481–7493,
746   https://doi.org/10.5194/acp-17-7481-2017, 2017.

747   Zhang, C., Lu, X., Zhai, J., Chen, H., Yang, X., Zhang, Q., Zhao, Q., Fu, Q., Sha, F.,
748   and Jin, J.: Insights into the formation of secondary organic carbon in the
749   summertime in urban Shanghai, J. Environ. Sci., article in press
750   https://doi.org/10.1016/j.jes.2017.12.018, 2018.

751   Zhang, G., Bi, X., He, J., Chen, D., Chan, L. Y., Xie, G., Wang, X., Sheng, G., Fu, J.,
752   and Zhou, Z.: Variation of secondary coatings associated with elemental carbon
753   by single particle analysis, Atmos. Environ., 92, 162–170,
754   https://doi.org/10.1016/j.atmosenv.2014.04.018, 2014.

755

756

Table 1. Number counts and fractions of the five types of BC-containing particles detected by the SPAMS.

Type	Number count of particles	Fraction of particles
Pure EC	5191	8.1%
KEC	21456	33.3%
NaKEC	11001	17.1%
ECOC	21225	33.0%
Others	5495	8.5%
Total BC-containing particles	64368	100%

757

758

759

760

761

762

763

764

765

766

767

Figure Captions

Figure 1. Schematic diagram of experimental setup.

Figure 2. Temporal profiles of gaseous pollutants (O_3, SO_2, CO, and NO_2), temperature, relative humidity (RH), and $PM_{2.5}$ and PM_{10} mass concentrations.

Figure 3. Averaged hygroscopic growth distributions of **(a)** total ambient particles and **(b)** BC particles at RH = 85% for three selected sizes (D_0=120 nm, 240 nm and 360 nm).

Figure 4. Diurnal variations of BC **(a)** number concentration and **(b)** number fraction (the ratio of the number concentration of BC particles to that of total particles at a certain D_0 and GF) for three selected size.

Figure 5. Diurnal variations of BC **(a)** core size and **(b)** coating thickness at different GFs.

Figure 6. Diurnal variations of number fraction of each classified particle type: **(a)** $G_{200-400}$: 200<d_{va}<400 nm and **(b)** $G_{400-800}$: 400<d_{va}<800 nm.

Figure 7. Averaged diurnal variations of O_x, SOC, SO_4^{2-} and NO_3^- mass concentration in **(a)**, **(b)**, **(c)** and **(d)**, respectively. The blue line in **(d)** is daily variation of relative peak area of NO_3^- measured by SPAMS.

Figure 8. Diurnal variations of relative peak area (RPA) of m/z +43 from ECOC type particles and the average aerodynamic particle size of ECOC particles.

789
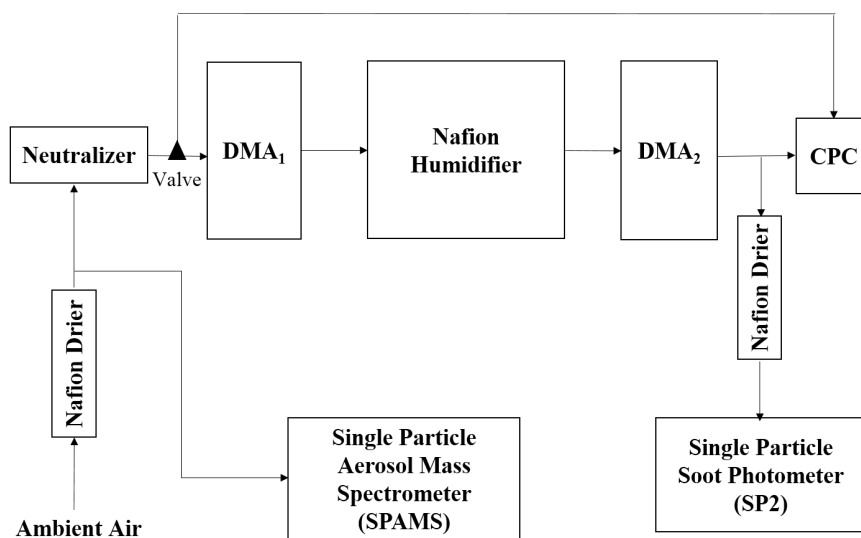
Figure 1. Schematic diagram of experimental setup.

791

792

793
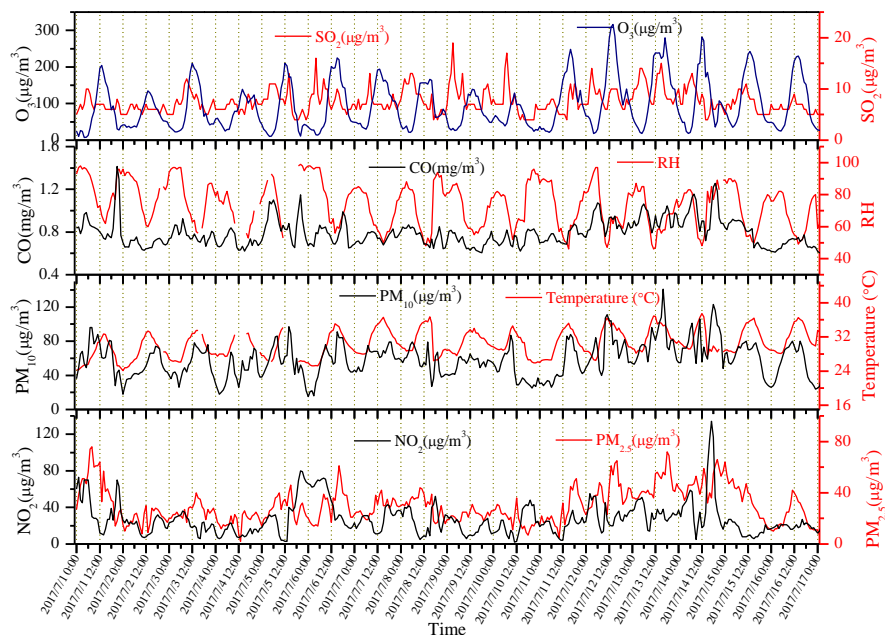
794

795

Figure 2. Temporal profiles of gaseous pollutants (O₃, SO₂, CO, and NO₂), temperature, relative humidity (RH), and PM₂.₅ and PM₁₀ mass concentrations.

798
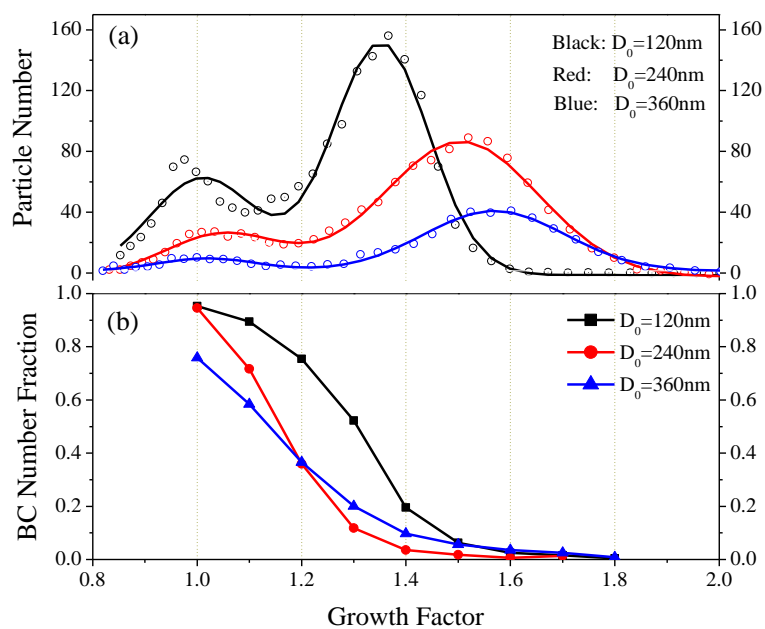
799
800

Figure 3. Averaged hygroscopic growth distributions of **(a)** total ambient particles
and **(b)** BC particles at RH = 85% for three selected sizes (D_0=120 nm, 240 nm and
360 nm).

804

805

806

807

808
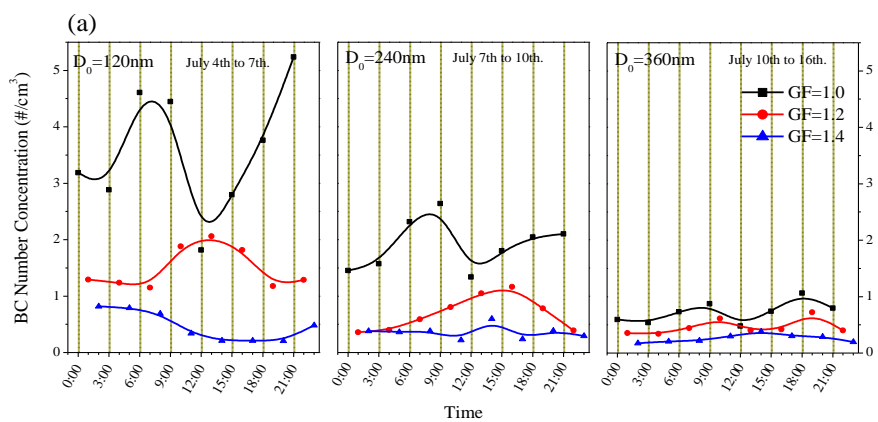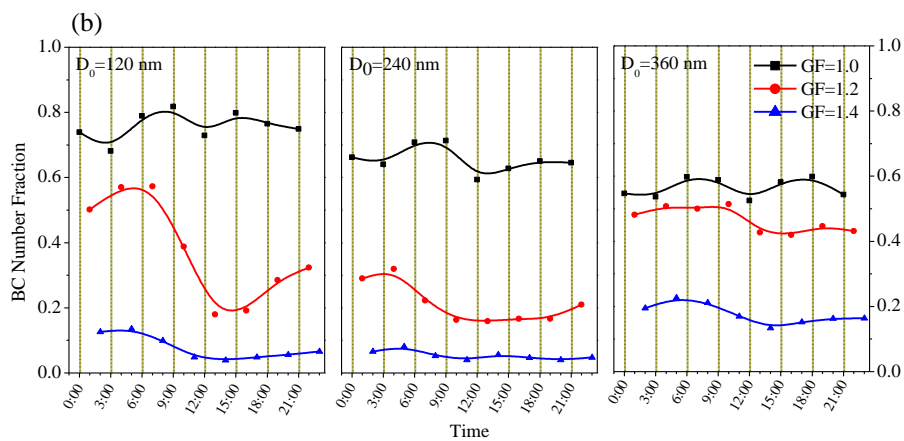
Figure 4. Diurnal variations of BC **(a)** number concentration and **(b)** number fraction

810   (the ratio of the number concentration of BC particles to that of total particles at a

811   certain D_0 and GF) for three selected size.
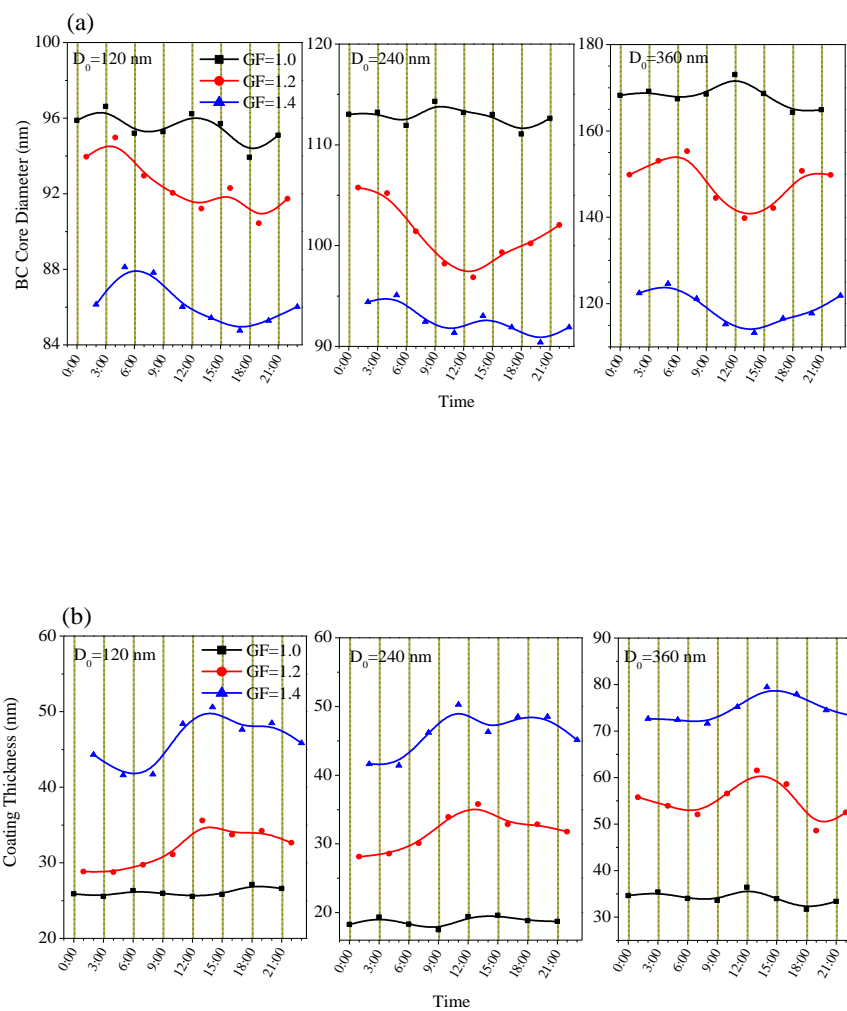
812

813
814

Figure 5. Diurnal variations of BC **(a)** core size and **(b)** coating thickness at different

GFs.

817

818

819
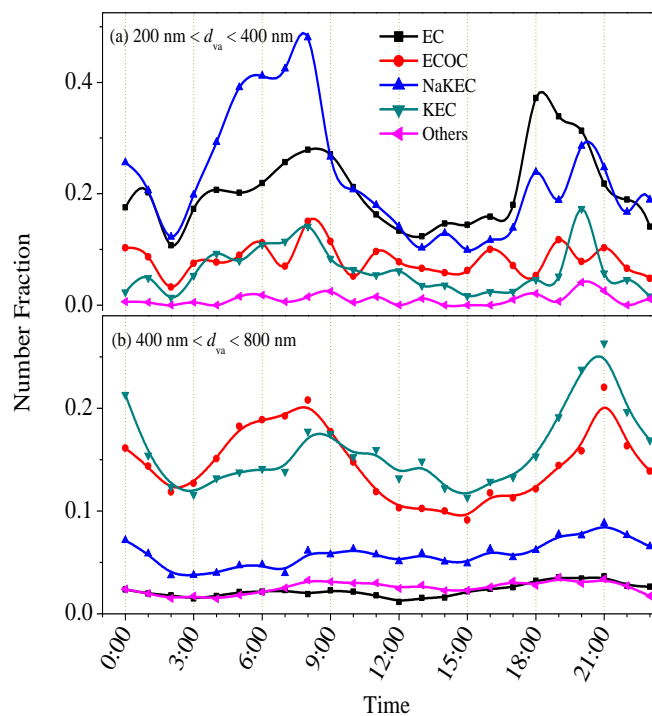
Figure 6. Diurnal variations of number fraction of each classified particle type: **(a)**
$G_{200\text{-}400}$: 200<d_{va}<400 nm and **(b)** $G_{400\text{-}800}$: 400<d_{va}<800 nm.

822

823

824

825

826

827
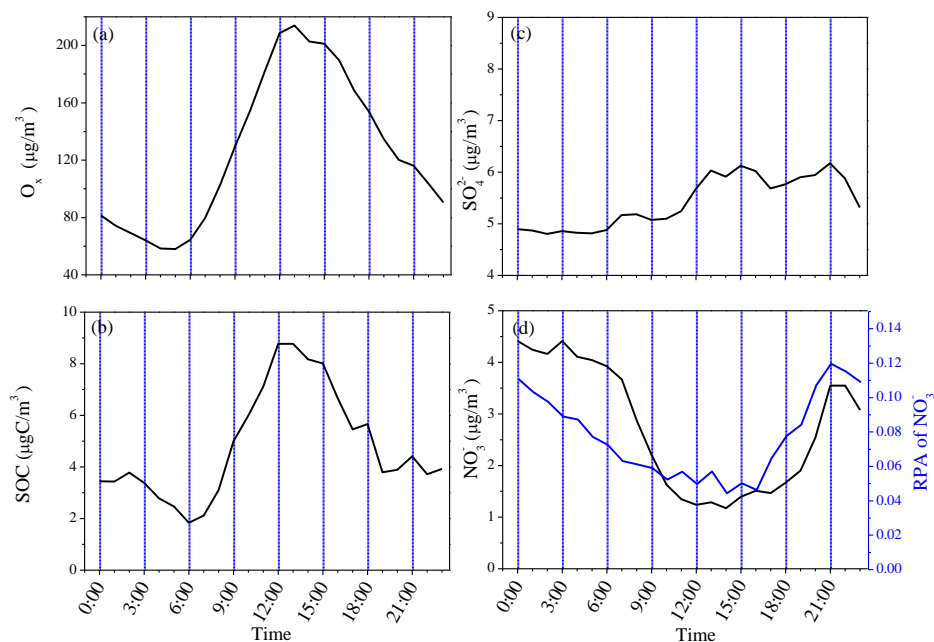
828
829

Figure 7. Averaged diurnal variations of O_x, SOC, SO_4^{2-} and NO_3^- mass concentration in **(a)**, **(b)**, **(c)** and **(d)**, respectively. The blue line in **(d)** is daily variation of relative peak area (RPA) of NO_3^- measured by SPAMS.

833

834

835
836
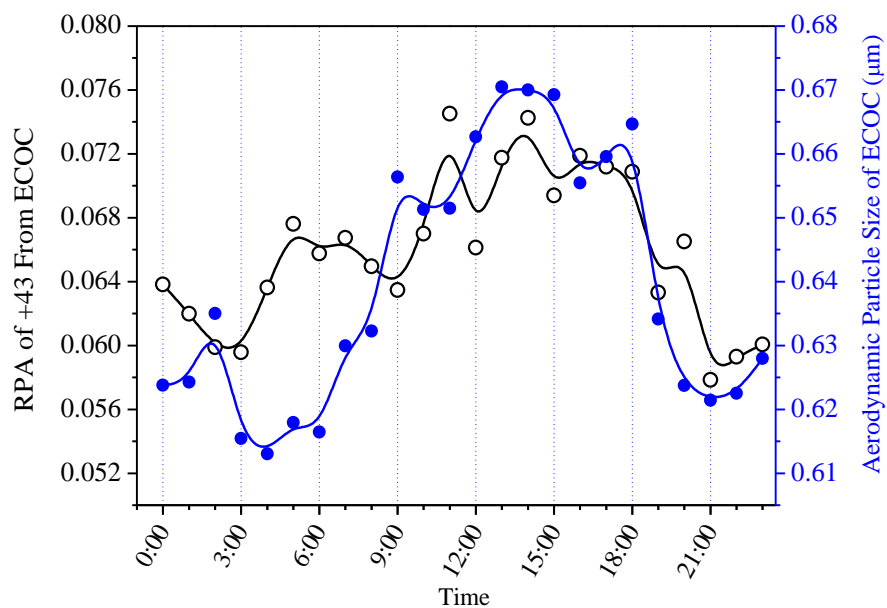
Figure 8. Diurnal variations of relative peak area (RPA) of m/z +43 from ECOC type

838 particles and the average aerodynamic particle size of ECOC particles.

839

840

841